



1 **A 16-year dataset (2000-2015) of high-resolution (3 hour, 10 km) global surface**
2 **solar radiation**

3 Wenjun Tang^{1,2}, Kun Yang^{3,2}, Jun Qin¹, Xin Li^{1,2}, and Xiaolei Niu¹

4 1. National Tibetan Plateau Data Center, Institute of Tibetan Plateau Research,
5 Chinese Academy of Sciences, Beijing 100101, China.

6 2. CAS Center for Excellence in Tibetan Plateau Earth Sciences, Chinese Academy of
7 Sciences, Beijing 100101, China.

8 3. Ministry of Education Key Laboratory for Earth System Modeling, Department of
9 Earth System Science, Tsinghua University, Beijing 100084, China.

10

11

12 Corresponding author and address:

13 Dr. Wenjun Tang

14 Institute of Tibetan Plateau Research, Chinese Academy of Sciences

15 Building 3, Courtyard 16, Lin Cui Road, Chaoyang District, Beijing 100101, China

16 Email: tangwj@itpcas.ac.cn

17 Tel: +86-10-84097046

18 Fax: +86-10-84097079



19 **Abstract:** The recent release of the International Satellite Cloud Climatology Project
20 (ISCCP) HXG cloud products and new ERA5 reanalysis data enabled us to produce a
21 global surface solar radiation (SSR) dataset: a 16-year (2000-2015) high-resolution (3
22 h, 10 km) global SSR dataset with an improved physical parameterization scheme.
23 The main inputs were cloud optical depth from ISCCP-HXG cloud products, the
24 water vapor, surface pressure and ozone from ERA5 reanalysis data, and albedo and
25 aerosol from Moderate Resolution Imaging Spectroradiometer (MODIS) products.
26 The estimated SSR data was evaluated against surface observations measured at 42
27 stations of the Baseline Surface Radiation Network (BSRN) and 90 radiation stations
28 of the China Meteorological Administration (CMA). Validation against the BSRN
29 data indicated that the mean bias error (MBE), root mean square error (RMSE) and
30 correlation coefficient (R) for the instantaneous SSR estimate at 10 km scale were
31 -11.5 W m^{-2} , 113.5 W m^{-2} , and 0.92, respectively. The error was clearly reduced when
32 the data were upscaled to 90 km; RMSE decreased to 93.4 W m^{-2} and R increased to
33 0.95. For daily SSR estimates at 90 km scale, the MBE, RMSE and R at the BSRN
34 were -5.8 W m^{-2} , 33.1 W m^{-2} and 0.95, respectively. These error metrics at the CMA
35 radiation stations were 2.1 W m^{-2} , 26.9 W m^{-2} and 0.95, respectively. Comparisons
36 with other global satellite radiation products indicated that our SSR estimates were
37 generally better than those of the ISCCP flux dataset (ISCCP-FD), the global energy
38 and water cycle experiment surface radiation budget (GEWEX-SRB), and the Earth's
39 Radiant Energy System (CERES). Our SSR dataset will contribute to the land-surface
40 process simulations and the photovoltaic applications in the future. The data set is
41 available at <https://doi.org/10.11888/Meteoro.tpsc.270112> (Tang, 2019).

42 **Keywords:** Surface solar radiation; Global product; High-resolution; Parameterization
43 scheme



44 **1. Introduction**

45 Surface solar radiation (SSR), which drives the energy, water and carbon cycles
46 of Earth's system, is the driving input for simulations of hydrology, ecology,
47 agriculture and land-surface processes (Wild, 2009; Wang et al., 2012). The accuracy
48 of SSR data influences simulations of runoff, gross primary productivity,
49 growth and yield of crops, and land data assimilation (Wild, 2012; Jia et al., 2013).
50 SSR is also an important variable that affects the speed of glacier melting (Yang et al.
51 2011). Variations of SSR also affect the rate of global warming and the change of pan
52 evaporation (Wild, et al., 2007; Qian et al., 2006).

53 Information on the spatiotemporal distribution of SSR is fundamental for
54 selection of sites for solar power plants, decisions on energy policy, optimization of
55 solar power systems, and operations management (Mondol et al., 2008; Sengupta et al.,
56 2018). To address issues such as these, historical SSR data has been obtained mainly
57 through ground-based observations, station-based estimates, and satellite-based
58 retrievals (Pinker & Laszlo, 1992; Li and Leighton, 1993; Liang et al., 2006; Zhang et
59 al., 2004; Wang et al. 2011; Huang et al., 2011; Kato et al., 2013; Ma & Pinker, 2012;
60 Zhang et al., 2014; Wang et al., 2015; Niu and Pinker, 2015).

61 Measurement by accurately calibrated and well-maintained radiometer of
62 pyranometer is the most effective method to obtain reliable long-term SSR data.
63 Although these data are valuable for simulations of land surface processes, solar
64 power applications and evaluation of satellite retrievals (Sengupta et al., 2018), the
65 high cost of maintaining radiation radiometers means that networks of radiation
66 stations are too sparsely distributed. However, networks of routine meteorological
67 stations are denser than those of radiation stations, and the variables observed at
68 routine meteorological stations can be used to estimate SSR. For example, based on



69 sunshine duration data, Tang et al. (2013, 2018) constructed long-term datasets of
70 both daily global radiation and direct radiation over China at more than 2400 routine
71 meteorological stations of the China Meteorological Administration (CMA). These
72 datasets are generally more accurate than those derived from satellite retrievals (Yang
73 et al., 2010). However, station-based estimates of SSR can be conducted only at
74 routine weather stations, many of which are sparsely distributed, often in remote
75 regions and harsh environment.

76 Alternatively, remote sensing retrievals based on satellites can provide reliable
77 spatiotemporally continuous SSR data, either globally or regionally. The many
78 methods that have been developed to retrieve SSR from satellite data can be roughly
79 divided into three types: empirical, semi-empirical and physical.

80 Empirical methods build function relationships between SSR measured at limited
81 numbers of stations and satellite data by applying regression or artificial intelligence
82 technology (Lu et al., 2011; Wei et al., 2019). Empirical methods may work well at
83 some locations, but the ability to expand their coverage to broader regions is limited.

84 Semi-empirical methods generally combine a physical model for clear-sky
85 conditions with an empirical scheme for cloudy conditions. A well-known
86 semi-empirical method is the Heliosat method of Cano et al. (1986), from which
87 several improved versions have since been developed (Hammer et al., 2003; Mueller
88 et al., 2009; Posselt et al., 2012; and Wang et al., 2014).

89 Physical methods are generally well-suited to generalization because they take
90 into account the physics processes of transfer of solar radiation from the top of the
91 atmosphere to the Earth's surface. The look-up table (LUT) and physical
92 parameterization methods (Pinker & Laszlo, 1992; Liang et al., 2006; Lu et al., 2010;
93 Qin et al., 2015; Xie et al., 2016; Huang et al., 2018) are two typical physical methods



94 that were widely used to estimate SSR from satellite data.

95 Several well-known global SSR datasets have been produced by physical
96 methods. These include the global energy and water cycle experiment surface
97 radiation budget (GEWEX-SRB, Pinker and Laszlo, 1992), the International Satellite
98 Cloud Climatology Project flux dataset (ISCCP-FD, Zhang et al., 2004) and the
99 Earth's Radiant Energy System (CERES) radiation products (Kato et al., 2013).
100 Although each of these have been widely used in various fields, the spatial resolutions
101 (≥ 100 km) of these SSR products is too coarse to meet the requirements of
102 high-resolution SSR data. A high-resolution (5 km, 1 h) global SSR product of the
103 Global Land Surface Satellite (GLASS) were recently released, but it contains data
104 spanning only three years. Tang et al. (2016) also produced a high-resolution SSR
105 product by combining data from polar-orbit and geostationary satellites, but the
106 product covers only China and the dataset spans only eight years.

107 The greatest uncertainty in satellite retrievals of SSR is the lack of a high-quality
108 cloud product, which severely limits the development of high-resolution, long-term
109 global satellite SSR products. However, the release in 2017 of new, global, long-term
110 ISCCP H-series cloud products at a spatial resolution of about 10 km has provided an
111 opportunity to develop a long-term high-resolution global-scale climate dataset of
112 SSR.

113 We developed a global-scale 16-year dataset (2000-2015) of SSR data from the
114 new ISCCP H-series cloud products and ERA5 reanalysis data, validated the accuracy
115 of this dataset with surface observations, and compared its performance with other
116 global satellite products. Section 2 introduces the method we used to estimate SSR.
117 Section 3 describes the input data we used for SSR estimation and the observations
118 data used for SSR validation. In Section 4, we presented our evaluation of the SSR



119 product and compared it with other satellites products. Data availability is given in
120 Section 5, and Section 6 presents some conclusions and explores future work to
121 further improve SSR products.

122

123 **2 Estimation of SSR**

124 The method we used to estimate SSR with ISCCP H-series cloud data is mainly
125 based on the SUNFLUX scheme, which was developed by Sun et al. (2012; 2014) and
126 first used by Tang et al. (2017) to retrieve SSR data from Moderate Resolution
127 Imaging Spectroradiometer (MODIS) atmospheric and land products. Their validation
128 of their results against measurements at BSRN stations indicated a mean root mean
129 square error (RMSE) of $\sim 90 \text{ W m}^{-2}$ for instantaneous SSR. Although Tang et al.
130 (2017) achieved higher accuracy than we did in this study (because the MODIS cloud
131 products they used are generally of better quality than the ISCCP H-series cloud data),
132 the instantaneous SSR they retrieved is slightly overestimated at most stations because
133 the original method they used only considers the effect of aerosol scattering on SSR,
134 but ignores the effect of aerosol absorption. To overcome this issue, we replaced the
135 aerosol parameterization scheme used by Tang et al. (2017) with that used by Qin et
136 al. (2015) and Tang et al. (2016). The resultant method is a pure physical
137 parameterization scheme with an efficient calculation speed. The inputs to the method
138 include cloud optical depth (COD) in the visible band, cloud cover, aerosol optical
139 depth (AOD), surface pressure, precipitable water, total ozone, surface albedo, and
140 carbon dioxide concentration (fixed at 375 ppm by volume). Detailed information
141 about the method is provided by Tang et al. (2017) and Tang et al. (2016).

142

143 **3 Data**



144 **3.1 Input data**

145 To produce the 16-years SSR products at global scale, we used three types of
146 input data.

147 The first of these was the level 2 ISCCP H-series cloud product HXG (H-series
148 pixel-level global, here called ISCCP-HXG), which is a globally merged product
149 generated based on the HGS (H-series gridded by satellite) product. The resolutions of
150 HXG are 3 h and 10 km, and the HXG cloud products are available for the period
151 from July 1983 to December 2015. Note that the ISCCP-HXG data are 0.1° gridded
152 snapshots (or instantaneous) available every 3 h not the average value over 3 h. More
153 information about the ISCCP-HXG cloud product is provided by Young et al. (2018).
154 Four variables were used in the ISCCP- HXG cloud product: cloud mask, VIS
155 retrieved liquid cloud optical depth, VIS retrieved ice cloud optical depth and cloud
156 top temperature. The cloud mask was used to distinguish clear-sky pixels from cloudy
157 pixels and the cloud top temperature was used to distinguish liquid cloud and ice
158 cloud.

159 The second data type we used was the new ERA5 reanalysis data. Three
160 variables of the ERA5 reanalysis data were used: surface pressure, total column water
161 vapor and total column ozone. The resolutions of the ERA5 reanalysis data are 1 h
162 and 25 km. To derive the same spatial resolution as the ISCCP- HXG cloud product,
163 we re-sampled the three variables of ERA5 reanalysis data to a spatial resolution of 10
164 km.

165 The third data type comprised aerosol and albedo data. The MODIS aerosol
166 (MOD08 or MYD08) and albedo (MCD43A3, Schaaf et al., 2002) products were used.
167 MOD and MYD denote product obtained from Terra and Aqua platforms,
168 respectively, and MCD indicates a combined product processed from both platforms



169 (King et al., 2003). The spatial resolution of MODIS aerosols and albedo data are
170 about 100 km and 5 km, respectively, so we re-sampled them both to 10 km. Missing
171 values in the MODIS aerosol and albedo products (included the period of 1 Jan 2000
172 to 23 Feb 2000) were replaced with the corresponding values of monthly mean
173 climatological data. Note that the use of climatological data to replace the real
174 information of aerosol and albedo would have introduced some uncertainty. Thus,
175 care should be taken when using the SSR dataset we derived for trend analysis.

176

177 **3.2 Validated data**

178 In this study, we used radiation observations made in 2009 to validate the
179 accuracy of the global-scale SSR estimate. These radiation observations were
180 collected at two networks. The first set was the radiation observations (with temporal
181 resolution of 1 minute) measured at 42 stations of Baseline Surface Radiation
182 Network (BSRN, Ohmura et al, 1998), which were marked as red crosses in Figure 1.
183 Radiation observations measured at BSRN stations are regarded as the most reliable
184 radiation data due to the instruments of highest available accuracy and careful
185 maintenance (see website: <https://bsrn.awi.de/>). To reduce uncertainty caused by
186 cosine response error of the pyranometers, we did not use the measured global
187 radiation data; instead we used the total of the measured direct and diffuse radiation to
188 evaluate the accuracy of the retrieved SSR.

189 The second set was the daily radiation observations measured at 90 CMA
190 radiation stations, which were denoted by black circles in Figure 1. Though the
191 pyranometers used to measure global radiation at CMA radiation stations were
192 calibrated by a series of standard procedures (Yang et al., 2008), the observed
193 radiation data collected at CMA radiation stations frequently include questionable



194 values, which may have been a result of improper operation of instruments and/or
195 instrument defects (Shi et al., 2008). To reduce the uncertainty caused by the
196 questionable radiation data, we used a quality-check procedure (Tang et al. 2010) to
197 exclude the spurious and erroneous measurements.

198

199 **4 Results and Discussion**

200 **4.1 Validation of estimated SSR against observations at BSRN stations**

201 Firstly, the estimated SSR were validated against the observations measured at
202 the 42 BSRN stations at both instantaneous and daily scales. To reduce the
203 uncertainties induced by broken clouds, we validated the estimated instantaneous SSR
204 against hourly mean observed ones centered on the time of satellite overpass,
205 according to the suggestion of Wang and Pinker (2009). To examine the effect of
206 different spatial resolutions on the accuracy of our SSR estimates, in addition to the
207 10 km spatial resolution, we also evaluated our estimated SSR at spatial resolutions of
208 30, 50, 70, 90 and 110 km derived by averaging the SSR values observed at the
209 original scale of 10 km.

210 Accuracy for instantaneous SSR at 90 km scale ($RMSE = 93.4 \text{ W m}^{-2}$, $R = 0.95$;
211 Fig. 2, Table 1) was clearly superior to that at 10 km scale ($RMSE = 113.5 \text{ W m}^{-2}$, $R =$
212 0.92), which may indicate that the surface observation points are generally
213 representative of more than 10 km, especially under cloudy conditions. Another
214 possible reason for this phenomenon would be caused by the time mismatch between
215 satellite observation and surface observation because the satellites do not take
216 instantaneous snapshots of the entire Earth. Generally, the last generation
217 geostationary satellites, such as the Geostationary Operational Environmental Satellite
218 (GOES), take about 30 min to scan the entire Earth. The averaging inherent in



219 upscaling of spatial resolution would tend to decrease these time mismatches.

220 To further illustrate this issue, the performances of our instantaneous SSR with
221 different spatial resolutions at the 42 BSRN stations were given in Table 1, which
222 suggests that the accuracy was clearly improved when the data were upscaled to 30
223 km, with a further slight improvement at 70 km, but that accuracy started to decrease
224 at 90 km. The performance of the ISCCP-FD was also presented in Table 1.
225 Apparently, the accuracy of our estimated instantaneous SSR is significantly higher
226 than that of the ISCCP-FD. A further advantage of our dataset is that its spatial
227 resolution is far higher than that of the ISCCP-FD products.

228 Figure 3 shows the spatial distribution of RMSE for the estimated instantaneous
229 SSR (spatial resolution 90 km) at all individual BSRN stations. The RMSE was < 90
230 $W m^{-2}$ at 30 of the 42 BSRN stations. RMSE values were between 90 and $105 W m^{-2}$
231 at five stations and $> 105 W m^{-2}$ at seven stations. The 12 stations where RMSE
232 values were $\geq 90 W m^{-2}$ are generally in coastal areas, on islands and in the
233 Antarctic polar region. Part of the reasons for these large error are the same as that
234 explained by Tang et al. (2017), who estimated instantaneous SSR with MODIS
235 level-2 land and atmospheric products. For example, the large RMSE value for station
236 IZA can be attributed to the poor representativeness of the station, which is located on
237 a mountain top, and this station point can not represent the satellite observations.
238 Another reason for the large RMSE values may be the uncertainties contained in the
239 inputs, especially uncertainties in cloud and aerosol data. The great uncertainties for
240 the MODIS AOD retrieval over coastal or island stations (Anderson et al, 2013)
241 would lead to large RMSE values at these stations. The large errors for the two
242 Antarctic stations (SYO and GVN) may reflect failure of cloud detection, which is
243 difficult over Antarctica region because the similarity of the properties of cloud and



244 surfaces snow over the Antarctica Pole, and because the temperature of cloud is
245 generally not lower than that of surface snow (Zhang et al. 2013).

246 Figure 4 presents the validation results for our estimated daily SSR at 42 BSRN
247 stations. The MBE values were -6.1 and 5.8 W m^{-2} for spatial resolutions of 10 and 90
248 km, respectively. The RMSE for 10 km was 38.0 W m^{-2} , and its value was decreased
249 to 33.1 W m^{-2} for 90 km. The R for 10 km was 0.93 and its value was increased to
250 0.95 for 90 km. Table 2 also lists the performances of our daily SSR estimate with
251 different spatial resolutions and the performance of the ISCCP-FD daily SSR product.
252 Our estimates of daily SSR at all spatial resolutions were clearly more accurate than
253 that of ISCCP-FD, and they obviously improved when upscaled to more than 30 km.

254 The spatial distribution of RMSE for our estimated daily SSR at spatial
255 resolution of 90 km (Fig. 5) showed that RMSE at most of the 42 BSRN stations were
256 $<35 \text{ W m}^{-2}$, although there were four stations with RMSE between 35 and 40 W m^{-2}
257 and six with RMSE $>40 \text{ W m}^{-2}$. These higher RMSE values may be attributed to lack
258 of representativeness for some stations, errors in the inputs and uncertainty of the
259 algorithm, similar to the reasons for the higher errors in our estimates of instantaneous
260 SSR.

261 GWEWX-SRB and CERES are two other well-known and widely used global
262 satellite radiation products. Zhang et al. (2013; fig. 8) evaluated the performance of
263 GEWEX-SRB SSR products with the mean 3-h observed data from the BSRN and
264 found that RMSEs for the instantaneous and daily SSR of GEWEX-SRB were 88.3
265 and 35.5 W m^{-2} , respectively. To compare our results with those derived from
266 GEWEX-SRB by Zhang et al. (2013), we re-evaluated our estimated SSR with the
267 mean 3-h observed data from the BSRN. The RMSEs for our estimated instantaneous
268 and daily SSR at 10 km spatial resolution were 108.1 and 36.5 W m^{-2} , respectively,



269 both of which are greater than those of GWEX-SRB. However, when we upscaled our
270 estimated SSR to 90 km scale, RMSEs for our instantaneous and daily SSR were
271 lower, 82.4 and 30.6 W m⁻², respectively, indicating that our estimates of SSR were
272 more accurate than those of GEWEX-SRB at the same spatial resolution. We also
273 compared the performance of our estimates of SSR with that of CERES
274 (SYN1deg_Ed4A, Fig. 6). The accuracies of CERES were generally higher than those
275 of ISCCP-FD at both instantaneous and daily scales, but obviously lower than those
276 of our estimates at all spatial resolutions from 10 to 110 km (Fig. 6 and Table 2).

277 Thus, our estimated SSR based on ISCCP-HXG cloud products provided a more
278 accurate, higher spatial resolution dataset than those of ISCCP-FD, GEWEX-SRB and
279 CERES products.

280

281 **4.2 Validation of estimated SSR against observations at 90 CMA radiation** 282 **stations**

283 Our estimated SSR were further evaluated against the observations collected at
284 the 90 CMA radiation stations at both daily and monthly scales. Figure 7 presents the
285 validation results for the estimated daily SSR at spatial resolutions of 10 and 90 km.
286 The MBE, RMSE and *R* for our estimated daily SSR at 10 km spatial resolution were
287 1.8 W m⁻², 32.4 W m⁻² and 0.93, respectively. Accuracy clearly improved for spatial
288 resolutions up to 90 km, for which the corresponding metrics were 2.1 W m⁻², 26.9 W
289 m⁻² and 0.95. The RMSE for our estimate of daily SSR at 10 km spatial resolution is
290 comparable to that of GEWEX-SRB daily SSR, which was also validated against
291 observations at the CMA radiation stations (RMSE 32.2 W m⁻²; see figure 7b of Qin
292 et al., 2015). However, the RMSE for the GEWEX-SRB daily SSR is clearly higher
293 than that of our estimate of daily SSR at 90 km spatial resolution, thus indicating that



294 the accuracy of our daily SSR estimates is superior to that of the GEWEX-SRB daily
295 SSR product at the same spatial resolution.

296 Table 3 shows that the accuracy of our estimates of daily SSR clearly improved
297 when upscaled to 30 km spatial resolution and were most accurate at 90 km spatial
298 resolution. RMSE and R (36.5 W m^{-2} and 0.91, respectively) for daily SSR of
299 ISCCP-FD show that our estimates are more accurate at all spatial resolutions. The
300 spatial distribution of RMSE for our daily SSR estimate at 90 km spatial resolution
301 was also given in Figure 8. Only nine CMA stations had $\text{RMSE} > 35 \text{ W m}^{-2}$ (Fig. 8);
302 most of these stations are in southern China where there is generally more cloud and
303 its distribution is more complicated than in other parts of China (Yu et al., 2001).

304 Figure 9 presents the validation results for our estimated monthly SSR. The MBE,
305 RMSE and R for our estimated monthly SSR at 10 km spatial resolution were 1.9 W
306 m^{-2} , 16.3 W m^{-2} and 0.97, and the corresponding values for 90 km were changed to
307 2.2 W m^{-2} , 14.9 W m^{-2} and 0.97. It can be clearly seen that the accuracy of the
308 ISCCP-FD monthly SSR are inferior to our estimated monthly SSR at scales from 10
309 to 110 km (Table 4).

310 The performances for CERES daily and monthly SSR were evaluated against
311 observations at the 90 CMA radiation stations (Fig. 10) and also compared with
312 those of our estimates from ISCCP-HXG (Table 4). The MBEs for CERES daily and
313 monthly SSR were greater than those of our estimates at all scales, and the RMSE
314 for CERES daily SSR was slightly smaller than that of our estimates at 10 km spatial
315 resolution, but obviously greater than our estimates at spatial resolutions from 30 to
316 110 km. The RMSE for CERES monthly SSR was greater than those of our
317 estimates at all scales. Thus, the accuracy of our estimates is generally higher than
318 that of CERES.



319

320 **4.3 Spatial distribution of the annual SSR**

321 Figure 11 presents the comparison of the global distribution of the annual mean
322 SSR in 2009 between our retrievals and the ISCCP-FD SSR product. From the figure,
323 it can be seen that the global distribution for our SSR estimate based on the ISCCP-
324 HXG cloud products is almost the same as that of the ISCCP-FD SSR product, but the
325 spatial resolution of our estimate is far higher than that of ISCCP-FD. There
326 is no doubt that we can get more details that the coarse resolution product ISCCP-FD
327 can not capture. For example, the region of high SSR clearly identified over the
328 Tibetan Plateau by our estimate (Fig. 11a) is barely discernible in the
329 ISCCP-FD-derived data (Fig. 11b). The high values are mainly from
330 around the equator and the low latitudes, and the low values mainly over the high
331 latitudes and the Arctic and Antarctic regions. This phenomenon is primarily
332 determined by the solar elevation angle. In addition, the relatively high values are also
333 found over the Bolivian Plateau, the Tibetan Plateau, and other high altitude regions
334 due to less radiative extinction over high altitudes.

335

336 **5 Data availability**

337 The 16-year dataset of global SSR is available at the National Tibetan Plateau
338 Data Center (<https://doi.org/10.11888/Meteoro.tpdc.270112>, Tang, 2019), Institute of
339 Tibetan Plateau Research, Chinese Academy of Sciences.

340

341 **6 Conclusions and Future work**

342 This study produced a 16-year (2000-2015) global dataset of SSR based on
343 recently updated ISCCP H-series cloud products, new ERA-5 reanalysis data and



344 MODIS albedo and aerosol products with a physically based retrieval scheme. The
345 retrieved SSR dataset was evaluated globally with observations collected at BRSN
346 and CMA radiation stations. To investigate the effect of spatial scale on the accuracy
347 of our estimated SSR dataset, our estimated SSR at spatial resolutions from 10 km to
348 110 km were validated. Validation against observed BSRN data showed MBEs of
349 -11.0 and 6.0 W m^{-2} for our estimates of instantaneous and daily SSR, respectively.
350 RMSEs for our instantaneous and daily SSR estimates at 10 km spatial resolution
351 were 113.5 and 38.0 W m^{-2} , respectively, but their accuracy clearly improved when
352 upscaled to more than 30 km spatial resolution. For example, the RMSEs decreased to
353 93.4 and 33.1 W m^{-2} when our estimates were upscaled from 10 to 90 km. The
354 accuracies of our SSR estimates were clearly higher than those of GEWEX-SRB,
355 ISCCP-FD and CERES products. At 10 km spatial resolution, validation of our daily
356 and monthly SSR estimates against observed data from CMA radiation stations
357 provided RMSEs of 32.4 and 16.3 W m^{-2} , respectively, but these values decreased to
358 26.9 and 14.9 W m^{-2} when our estimates were upscaled to 90 km spatial resolution.
359 The errors of our SSR estimates when validated against observed data from CMA
360 were also lower than those of GEWEX-SRB, ISCCP-FD and CERES products. We
361 attributed large errors in our estimates at some stations to the lack of
362 representativeness of some stations, uncertainties in the input data, such as cloud
363 detection failures at stations in polar regions, large uncertainties in MODIS AOD
364 retrievals over stations in coastal areas and on islands, and uncertainty in the retrieval
365 scheme we used. However, the retrieval scheme we used worked well at most of the
366 stations used in our study despite their considerable geographic and climatologic
367 differences.

368 The spatial resolution and accuracy of the new dataset are both higher than those



369 of the global satellite radiation products of GEWEX-SRB, ISCCP-FD, and CERES
370 and will contribute to photovoltaic applications and research related to simulation of
371 land surface processes. When reliable global aerosol and albedo datasets become
372 available, we intend to expand our dataset of SSR estimates back to mid-1983. We
373 also plan to expand the dataset beyond 2015 by using SSR estimates from
374 new-generation geostationary satellites.

375

376 **Author contributions.** All authors discussed the results and contributed to the
377 manuscript. WT calculated the dataset, analyzed the results, and drafted the
378 manuscript.

379

380 **Competing interests.** The authors declare that they have no conflict of interest.

381

382 **Acknowledgments.** The CMA radiation station data were obtained from the National
383 Meteorological Information Center (NMIC) and. The ISCCP-HXG cloud products
384 were obtained from the NOAA's National Centers for Environmental Information
385 (NCEI). The ERA5 reanalysis data and MODIS albedo and aerosol data were
386 downloaded from official websites (<https://www.ecmwf.int> and
387 <https://ladsweb.modaps.eosdis.nasa.gov>). The authors would like to thank the
388 Baseline Surface Radiation Network (BSRN) observation teams for their maintenance
389 work.

390

391 **Financial support.** This work was supported by the National Key Research and
392 Development Program of China (Grants No. 2018YFA0605400 and
393 2017YFA0603604), the National Natural Science Foundation of China (Grants No.



394 41671372), the Youth Innovation Promotion Association CAS (No. 2017100),
395 and the 13th Five-year Informatization Plan of Chinese Academy of Sciences
396 (Grant No. XXH13505-06), and the Strategic Priority Research Program of Chinese
397 Academy of Sciences (Grant No.XDA20100102).

398

399 **References**

- 400 Anderson, J. C., Wang, J., Zeng, J., Leptoukh, G., Petrenko, M., Ichoku, C. and Hu, C.:
401 Long-term statistical assessment of Aqua-MODIS aerosol optical depth over
402 coastal regions: bias characteristics and uncertainty sources, *Tellus B: Chemical
403 and Physical Meteorology*, 65:1, 20805, DOI: 10.3402/tellusb.v65i0.2080, 2013.
- 404 Cano, D., Monget, J. M., Albuissou, M., Guillard, H., Regas, N. and Wald, L.: A
405 method for the determination of the global solar radiation from meteorological
406 satellite data, *Sol. Energy*, 37(1), 31–39, doi:10.1016/0038-092X(86)90104-0,
407 1986.
- 408 Hammer, A., Heinemann, D., Hoyer, C., Lorenz, E., Muller, R. and Beyer, H. G.:
409 Solar energy assessment using remote sensing technologies, *Remote Sens.
410 Environ.*, 86(3), 423–432, doi:10.1016/S0034-4257(03)00083-X, 2003.
- 411 Huang, G., Ma, M., Liang, S., Liu, S., and Li, X.: A LUT-based approach to estimate
412 surface solar irradiance by combining MODIS and MTSAT data, *J. Geophys.
413 Res.*, 116, D22201, doi:10.1029/2011JD016120, 2011.
- 414 Huang, G., Liang, S., Lu, N., Ma, M., and Wang, D.: Toward a broadband
415 parameterization scheme for estimating surface solar irradiance: Development
416 and preliminary results on MODIS products. *Journal of Geophysical Research:
417 Atmospheres*, 123, 12,180–12,193. <https://doi.org/10.1029/2018JD028905>,
418 2018.



- 419 Jia, B., Xie, Z., Dai, A., Shi, C., and Chen, F.: Evaluation of satellite and reanalysis
420 products of downward surface solar radiation over East Asia: Spatial and
421 seasonal variations, *J. Geophys. Res. Atmos.*, 118, 3431–3446,
422 doi:10.1002/jgrd.50353, 2013.
- 423 Kato, S., Loeb, N.G., Rose, F.G., Doelling, D.R., Rutan, D.A., Caldwell, T.E., et al.:
424 Surface irradiances consistent with CERES-derived top-of-atmosphere
425 shortwave and longwave irradiances, *Journal of Climate*, 26, 2719–2740, 2013.
- 426 King, M. D., et al.: Cloud and aerosol properties, perceptible water, and profiles of
427 temperature and humidity from MODIS, *IEEE Trans. Geosci. Remote Sens.*, 41,
428 442–458, doi:10.1109/TGRS.2002.808226, 2003.
- 429 Li, Z. Q., and Leighton, H. G.: Global climatologies of solar radiation budgets at the
430 surface and in the atmosphere from 5 years of ERBE data, *J. Geophys. Res.* 98,
431 4919–4930, 1993.
- 432 Liang, S., Zheng, T., Liu, R. G., Fang, H. L., Tsay, S. C., and Running, S.: Estimation
433 of incident photosynthetically active radiation from Moderate Resolution
434 Imaging Spectrometer data, *J. Geophys. Res.*, 111, D15208,
435 doi:10.1029/2005JD006730, 2006.
- 436 Lu N., Liu R., Liu J., Liang, S.: An algorithm for estimating downward shortwave
437 radiation from GMS 5 visible imagery and its evaluation over China, *J. Geophys.*
438 *Res.*, 115(D18102), doi:10.1029/2009JD013457, 2010.
- 439 Lu N., Qin J., Yang K., and Sun, J.: A simple and efficient algorithm to estimate daily
440 global solar radiation from geostationary satellite data, *Energy*, 36, 3179–3188,
441 doi:10.1016/j.energy.2011.03.007, 2011.
- 442 Ma, Y. and Pinker, R. T.: Modeling shortwave radiative fluxes from satellites, *J.*
443 *Geophys. Res.*, 117, D23202, doi:10.1029/2012JD18332,1–19, 2012.



- 444 Mondol J. D., Yohanis Y. G., Norton B.: Solar radiation modelling for the simulation
445 of photovoltaic systems, *Renew. Energy*, 33(5), 1109–1120, 2008.
- 446 Mueller, R., Matsoukas, C., Gratzki, A., Behr, H., and Hollmann, R.: The CM-SAF
447 operational scheme for the satellite based retrieval of solar surface irradiance—A
448 LUT based eigenvector hybrid approach, *Remote Sens. Environ.*, 113(5), 1012 –
449 1024, doi:10.1016/j.rse.2009.01.012, 2009.
- 450 Niu, X., and Pinker, R. T.: An improved methodology for deriving high-resolution
451 surface shortwave radiative fluxes from MODIS in the Arctic region, *J. Geophys.*
452 *Res. Atmos.*, 120, 2382–2393, doi:10.1002/2014JD022151, 2015.
- 453 Ohmura, A., et al.: Baseline Surface Radiation Network (BSRN/WCRP): New
454 precision radiometry for climate change research, *Bull. Am. Meteorol. Soc.*, 79,
455 2115 – 2136, doi:10.1175/1520-0477(1998)079<2115:BSRNBW>2.0.CO;2,
456 1998.
- 457 Pinker, R. T., and Laszlo, I.: Modeling surface solar irradiance for satellite application
458 on a global scale, *J. Appl. Meteorol.*, 31, 194–211,
459 doi:10.1175/1520-0450(1992)031<0194:MSSIFS>2.0.CO;2, 1992.
- 460 Posselt, R., Mueller, R., Stöckli, R., and Trentmann, J.: Remote sensing of solar
461 surface radiation for climate monitoring—The CM-SAF retrieval in international
462 comparison, *Remote Sens. Environ.*, 118, 186–198, 2012.
- 463 Qian, Y., Kaiser, D.P., Leung, L.R., and Xu, M.: More frequent cloud-free sky and less
464 surface solar radiation in China from 1955 to 2000. *Geophys Res. Lett.* 33,
465 L01812, 2006.
- 466 Qin, J., Tang, W., Yang, K., Lu, N., Niu, X., and Liang, S.: An efficient physically
467 based parameterization to derive surface solar irradiance based on satellite
468 atmospheric products, *J. Geophys. Res. Atmos.*, 120, 4975–4988,



- 469 doi:10.1002/2015JD023097, 2015.
- 470 Schaaf, C. B., et al.: First operational BRDF, albedo nadir reflectance products from
471 MODIS, Remote Sens. Environ., 83, 135–148,
472 doi:10.1016/S0034-4257(02)00091-3, 2002.
- 473 Sengupta, M., Xie, Y., Lopez, A., Habte, A., Maclaurin, G., and Shelby, J.: The
474 national solar radiation data base (NSRDB). *Renew. Sustain. Energy Rev.* 89,
475 51–60. [https:// doi.org/10.1016/j.rser.2018.03.003](https://doi.org/10.1016/j.rser.2018.03.003), 2018.
- 476 Shi, G.Y., Hayasaka, T., Ohmura, A., Chen, Z.H., Wang, B., Zhao, J.Q., Che, H.Z.,
477 and Xu, L.: Data quality assessment and the long-term trend of ground solar
478 radiation in China. *J. Appl. Meteor. Climatology* 47, 1006–1016, 2008.
- 539 Sun, Z., Liu, J., Zeng, X., and Liang, H.: Parameterization of instantaneous global
540 horizontal irradiance: Cloudy sky component, *J. Geophys. Res.*, 117, D14202,
541 doi:10.1029/2012JD017557, 2012.
- 542 Sun Z., Zeng X., Liu J., Liang H., Li J.: Parametrization of instantaneous global
543 horizontal irradiance: clear-sky component, *Q. J. R. Meteorol. Soc.* 140:
544 267–280. DOI:10.1002/qj.2126, 2014.
- 545 Tang W.: A 16-year dataset of high-resolution (3 hour, 10 km) global surface solar
546 radiation (2000-2015), *Big Data System for Pan-Third Pole*, doi:
547 10.11888/Meteoro.tpdc.270112, 2019.
- 548 Tang, W., Yang, K., He, J., and Qin, J.: Quality control and estimation of global solar
549 radiation in China, *Sol. Energy*, 84, 466–475, 2010.
- 550 Tang, W., Qin, J., Yang, K., Niu, X., Zhang, X., Yu Y., and Zhu X.: Reconstruction of
551 Daily Photosynthetically Active Radiation and its Trends over China, *J. Geophys.*
552 *Res. Atmos.*, 118(23), 13,292-13,302, doi:10.1002/2013JD020527, 2013.
- 553 Tang, W., Qin, J., Yang, K., Liu, S., Lu, N., and Niu, X.: Retrieving high-resolution



- 554 surface solar radiation with cloud parameters derived by combining MODIS and
555 MTSAT data, *Atmos. Chem. Phys.*, 16, 2543-2557,
556 doi:10.5194/acp-16-2543-2016, 2016.
- 557 Tang, W., Yang, K., Sun, Z., Qin, J., and Niu, X.: Global Performance of a Fast
558 Parameterization Scheme for Estimating Surface Solar Radiation From MODIS
559 Data, *IEEE Trans. Geosci. Remote Sens.*, 55(6), 3558-3571,
560 doi:10.1109/TGRS.2017.2676164, 2017.
- 561 Tang, W., Yang, K., Qin, J., Min, M., and Niu, X.: First effort for constructing a direct
562 solar radiation data set in China for solar energy applications. *Journal of*
563 *Geophysical Research: Atmospheres*, 123, 1724–1734.
564 <https://doi.org/10.1002/2017JD028005>, 2018.
- 565 Wang, H., and Pinker, R. T.: Shortwave radiative fluxes from MODIS: Model
566 development and implementation, *J. Geophys. Res.*, 114, D20201,
567 doi:10.1029/2008JD010442, 2009.
- 568 Wang, K. C., Dickinson, R. E., Wild, M., and Liang, S.: Atmospheric impacts on
569 climatic variability of surface incident solar radiation, *Atmos. Chem. Phys.*, 877
570 12(20), 9581-9592, 2012.
- 571 Wang, K.C., Ma, Q., Li, Z., and Wang, J.: Decadal variability of surface incident solar
572 radiation over China: Observations, satellite retrievals, and reanalyses,
573 *J.Geophys.Res.Atmos.*, 120(13), 6500-6514, 2015.
- 574 Wang, P., Stammes, P., and Mueller, R.: Surface solar irradiance from SCIAMACHY
575 measurements: Algorithm and validation, *Atmos. Meas. Tech.*, 4, 875 - 891,
576 <http://dx.doi.org/10.5194/amt-4-875-2011>, 2011.
- 577 Wang, P., Sneep, M., Veefkind, J.P., Stammes, P., and Levelt, P.F.: Evaluation of
578 broadband Surface solar irradiance from the Ozone Monitoring Instrument,



- 579 Remote Sens. Environ., 149, 88 – 99, <http://dx.doi.org/10.1016/j.rse.2014.03.036>,
580 2014.
- 581 Wei, Y., Zhang, X., Hou, N., Zhang, W., Jia, K., and Yao, Y.: Estimation of surface
582 downward shortwave radiation over China from AVHRR data based on four
583 machine learning methods, *Sol. Energy*, 177, 32–46, 2019.
- 584 Wild, M., Ohmura, A., and Makowski, K.: Impact of global dimming and brightening
585 on global warming. *Geophys. Res. Lett.*, 34, L04702,
586 doi:10.1029/2006GL028031, 2007.
- 587 Wild, M.: Global dimming and brightening: A review, *J. Geophys. Res. Atmos.*, 888 114,
588 D00D16, 2009.
- 589 Wild, M.: Enlightening global dimming and brightening, *Bull. Am. Meteorol. Soc.*,
590 93(1), 27–37, 2012.
- 591 Xie, Y., Sengupta, M., and Dudhia, J.: A Fast All-sky Radiation Model for Solar
592 applications (FARMS): algorithm and performance evaluation. *Sol. Energy* 135,
593 435–445, 2016.
- 594 Yang, K., He, J., Tang, W., Qin, J., and Cheng, C.: On downward shortwave and
595 longwave radiations over high altitude regions: Observation and modeling in the
596 Tibetan Plateau, *Agric. For. Meteorol.*, 150(1), 38–46,
597 doi:10.1016/j.agrformet.2009.08.004, 2010.
- 598 Yang, W., Guo, X., Yao, T., Yang, K., Zhao, L., Li, S., and Zhu, M.: Summertime
599 surface energy budget and ablation modeling in the ablation zone of a maritime
600 Tibetan glacier, *J. Geophys. Res.*, 116, D14116, doi:10.1029/2010JD015183,
601 2011.
- 602 Yang, Y., Wang, D., Lv, W. H., Mo, Y. Q., and Ding, L.: Solar radiation standard and
603 its values transfer system in China, available at:



604 [http://www.knmi.nl/samenw/geoss/wmo/TECO2008/IOM-96-TECO2008/P1\(52\)](http://www.knmi.nl/samenw/geoss/wmo/TECO2008/IOM-96-TECO2008/P1(52))
605 [_Yang_China.pdf](#), 2008.

606 Young, A.H., Knapp, K.R., Inamdar, A., Hankinns,W., and Rossow,W.B.: The
607 International Cloud Climatology Project H-Series climate data record product.
608 Earth Syst. Sci. Data, 10, 583–593, 2018.

609 Yu, R. C., Yu, Y. Q. and Zhang, M. H.: Comparing cloud radiative properties between
610 the eastern China and the Indian monsoon region, Adv. Atmos. Sci., 18 (6),
611 1090–1102, 2001.

612 Zhang, T., Stackhouse Jr., P. W., Gupta, S. K., Cox, S. J., Mikovitz, J. C., and
613 Hinkelman, L. M.: The validation of the GEWEX SRB surface shortwave flux
614 data products using BSRN measurements: A systematic quality control,
615 production and application approach, J. Quant. Spectrosc. Radiat. Transfer, 122,
616 127–140, doi:10.1016/j.jqsrt.2012.10.004, 2013.

617 Zhang, X., Liang, S., Zhou, G., Wu, H., and Zhao, X.: Generating Global LAnd
618 Surface Satellite incident shortwave radiation and photosynthetically active
619 radiation products from multiple satellite data, Remote Sens. Environ., 152, 318
620 – 332, 2014.

621 Zhang Y. C., Rossow W. B., Lacis A. L., Valdar, o., Michael, I. M.: Calculation of
622 radiative fluxes from the surface to top of atmosphere based on ISCCP and other
623 global data sets: refinements of the radiative transfer model and the input data, J.
624 Geophys. Res., 109, D19105, doi:10.1029/2003JD004457, 2004.

625
626



627 **Figure captions**

628 **Figure 1** Distribution of radiation measurement stations used to evaluate the
629 performance of the estimated SSR. The blue circles mark the locations of
630 the 90 CMA radiation stations, and the red crosses mark those of the 42
631 BSRN stations. Note that two stations (labeled as DAR and DWN) in
632 Australia and two stations (labeled as BIL and E13) in America are very
633 close to each other.

634 **Figure 2** Comparisons of our estimated instantaneous SSR at spatial resolutions of (a)
635 10 km and (b) 90 km with observed SSR for 42 BSRN stations.

636 **Figure 3** Spatial distribution of RMSE ($W m^{-2}$) for our estimated instantaneous SSR
637 (spatial resolution 90 km) at 42 BSRN stations.

638 **Figure 4** Comparisons of our estimated daily SSR at spatial resolutions of (a) 10 km
639 and (b) 90 km with observed SSR for 42 BSRN stations.

640 **Figure 5** Spatial distribution of RMSE ($W m^{-2}$) for our estimated daily SSR (spatial
641 resolution 90 km) at 42 BSRN stations.

642 **Figure 6** Comparison of CERES SSR products with observed SSR at 42 BSRN
643 stations for both (a) instantaneous and (b) daily scales.

644 **Figure 7** Comparisons of our estimated daily SSR at spatial resolutions of (a) 10 km
645 and (b) 90 km with observed SSR at 90 CMA radiation stations.

646 **Figure 8** Spatial distribution of RMSE ($W m^{-2}$) for our estimated daily SSR (spatial
647 resolution 90 km) at 90 CMA radiation stations.

648 **Figure 9** Comparisons of our estimated monthly SSR at spatial resolutions of (a) 10
649 km and (b) 90 km with observed monthly SSR at 90 CMA radiation
650 stations.

651 **Figure 10** Comparison of CERES (a) daily and (b) monthly SSR products with those

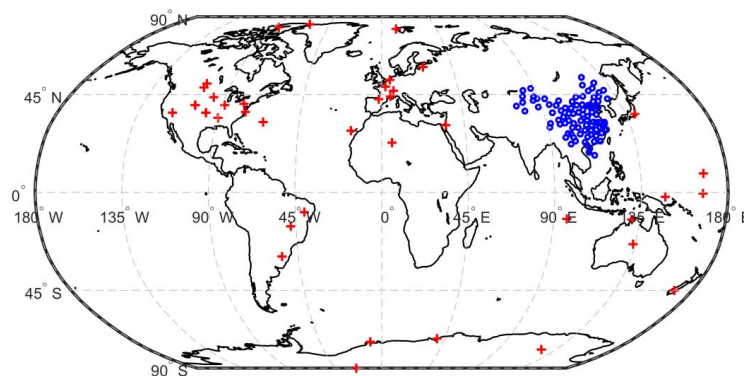


652 observed at 90 CMA stations.

653 **Figure 11** Spatial distribution of global annual mean SSR (W m^{-2}) of (a) ISCCP-HXG

654 and (b) ISCCP-FD in 2009.

655

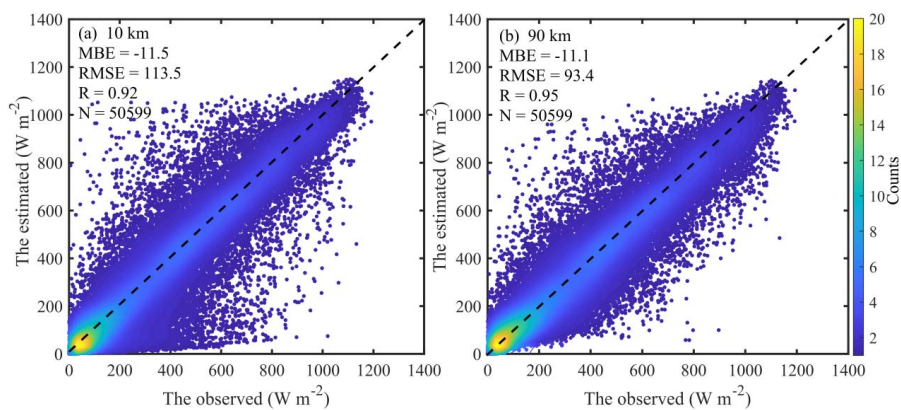


656

657 **Figure 1** Distribution of radiation measurement stations used to evaluate the
658 performance of the estimated SSR. The blue circles mark the locations of
659 the 90 CMA radiation stations, and the red crosses mark those of the 42
660 BSRN stations. Note that two stations (labeled as DAR and DWN) in
661 Australia and two stations (labeled as BIL and E13) in America are very
662 close to each other.

663

664



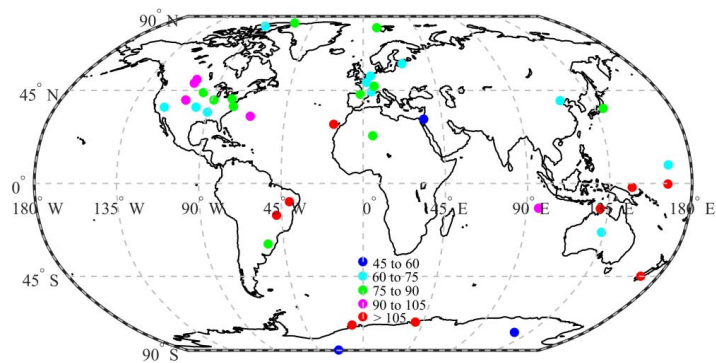
665

666 **Figure 2** Comparisons of our estimated instantaneous SSR at spatial resolutions of (a)

667

10 km and (b) 90 km with observed SSR for 42 BSRN stations.

668

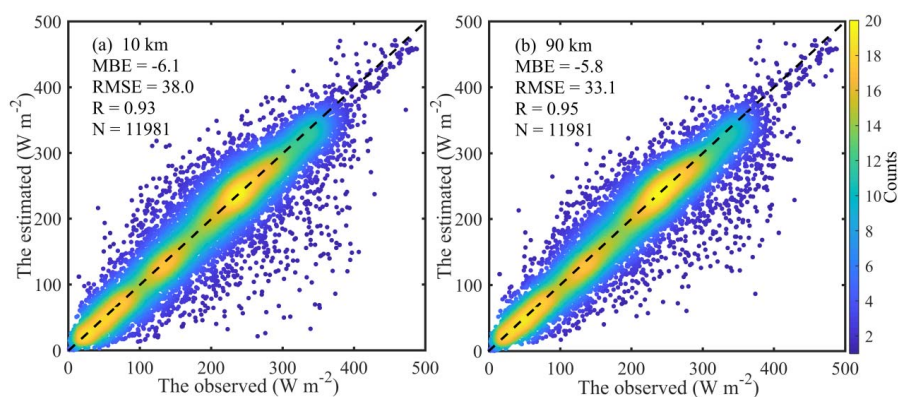


669

670 **Figure 3** Spatial distribution of RMSE ($W m^{-2}$) for our estimated instantaneous SSR

671 (spatial resolution 90 km) at 42 BSRN stations.

672

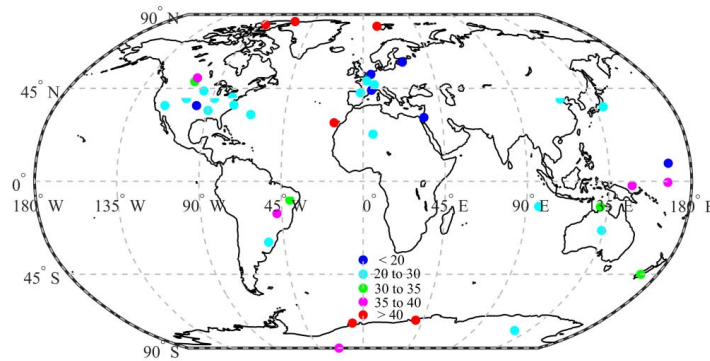


673

674 **Figure 4** Comparisons of our estimated daily SSR at spatial resolutions of (a) 10 km

675 and (b) 90 km with observed SSR for 42 BSRN stations.

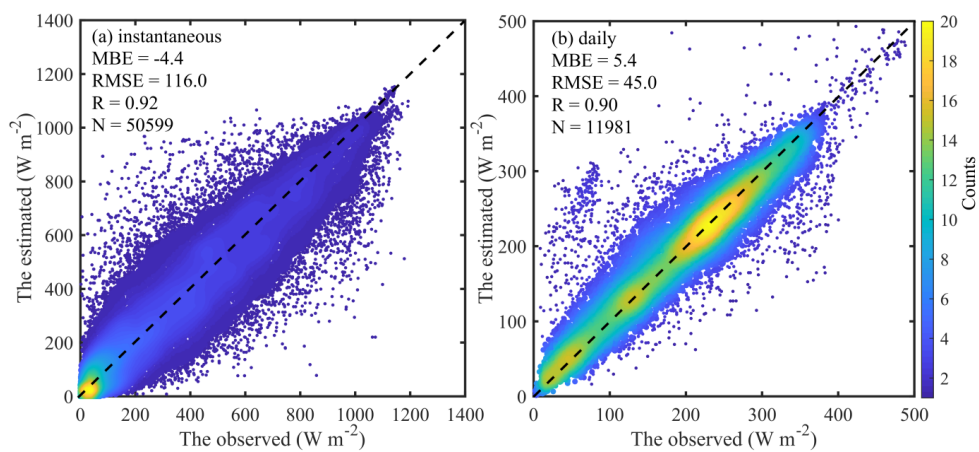
676



677

678 **Figure 5** Spatial distribution of RMSE (W m^{-2}) for our estimated daily SSR (spatial
679 resolution 90 km) at 42 BSRN stations.

680



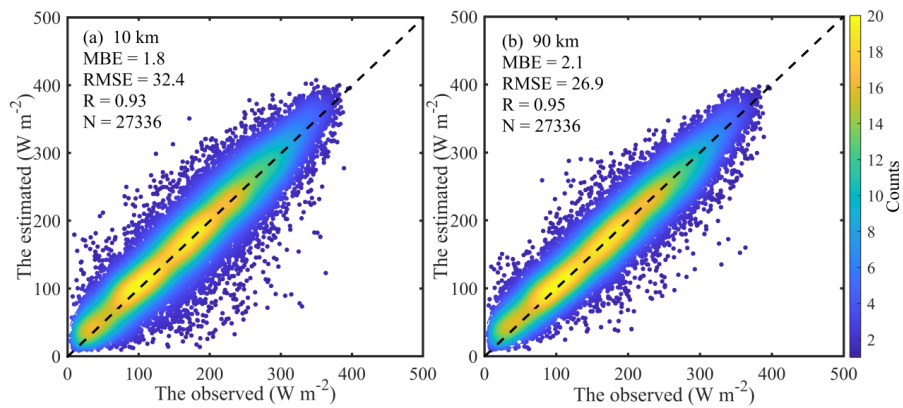
681

682 **Figure 6** Comparison of CERES SSR products with observed SSR at 42 BSRN

683 stations for both (a) instantaneous and (b) daily scales.

684

685



686

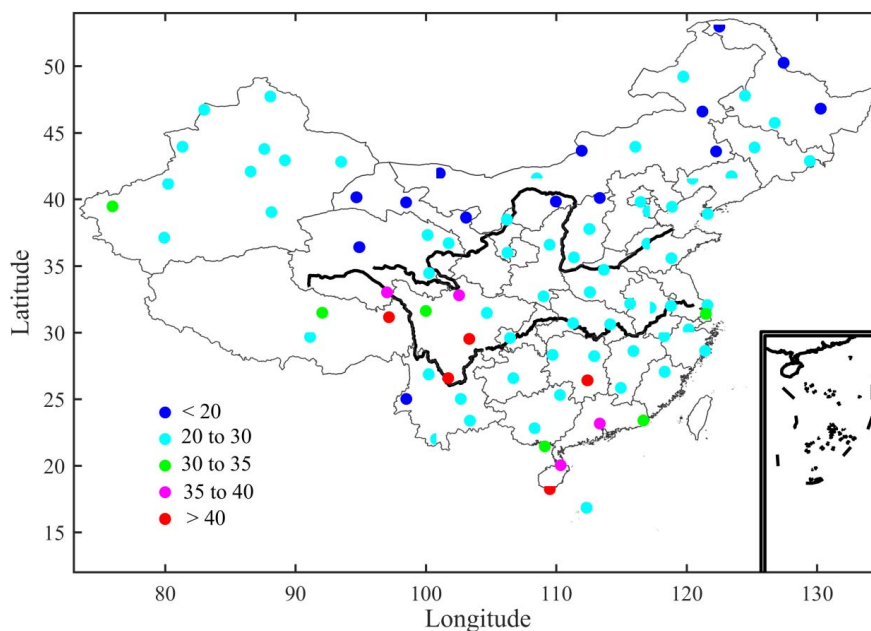
687 **Figure 7** Comparisons of our estimated daily SSR at spatial resolutions of (a) 10 km

688 and (b) 90 km with observed SSR at 90 CMA radiation stations.

689

690

691

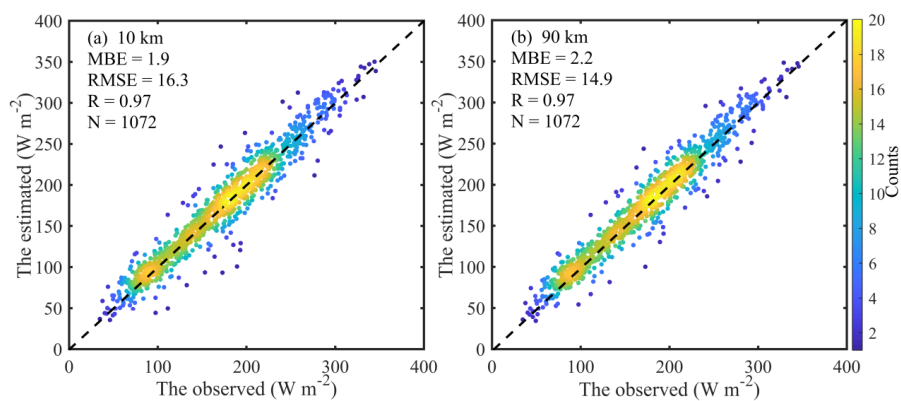


692

693 **Figure 8** Spatial distribution of RMSE (W m^{-2}) for our estimated daily SSR (spatial
694 resolution 90 km) at 90 CMA radiation stations.

695

696



697

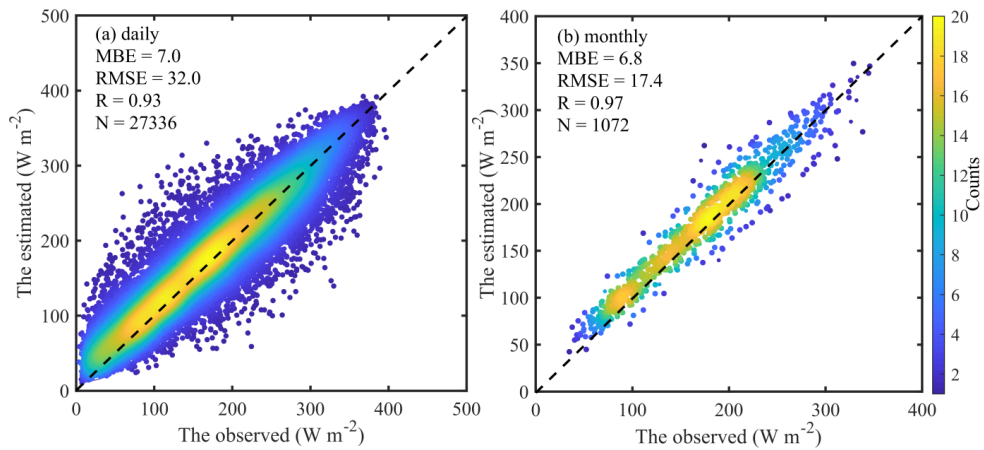
698 **Figure 9** Comparisons of our estimated monthly SSR at spatial resolutions of (a) 10

699 km and (b) 90 km with observed monthly SSR at 90 CMA radiation

700 stations.

701

702

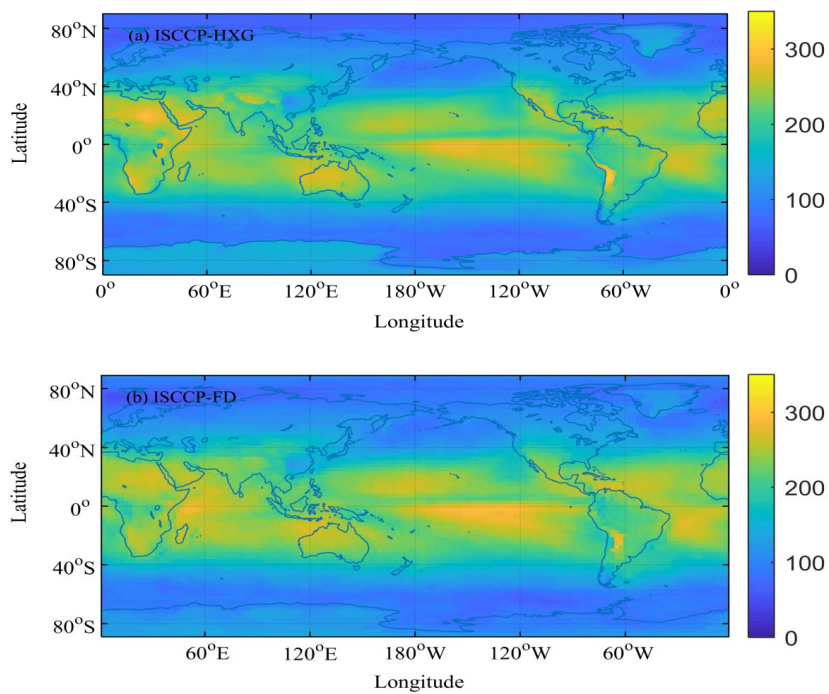


703

704 **Figure 10** Comparison of CERES (a) daily and (b) monthly SSR products with those
705 observed at 90 CMA stations.

706

707



708

709 **Figure 11** Spatial distribution of global annual mean SSR (W m^{-2}) of (a) ISCCP-HXG

710 and (b) ISCCP-FD in 2009.

711

712



713 **Table 1.** Effect of spatial resolution on accuracy of our estimated instantaneous SSR
714 compared to observations at the 42 BSRN stations. A comparisons with
715 instantaneous SSR of ISCCP-FD is also shown.

	Spatial resolution	MBE (W m^{-2})	RMSE (W m^{-2})	<i>R</i>
ISCCP-HXG	10 km	-11.5	113.5	0.92
ISCCP-HXG	30 km	-11.0	96.5	0.94
ISCCP-HXG	50 km	-11.3	93.5	0.95
ISCCP-HXG	70 km	-11.3	93.2	0.95
ISCCP-HXG	90 km	-11.1	93.4	0.95
ISCCP-HXG	110 km	-11.4	94.3	0.95
ISCCP-FD	280 km	-11.2	131.4	0.89

716



717 **Table 2.** Effect of spatial resolution on accuracy of our estimated daily SSR compared
718 to observations at 42 BSRN stations. A comparisons with daily SSR of
719 ISCCP-FD is also shown.

	Spatial resolution	MBE (W m^{-2})	RMSE (W m^{-2})	R
ISCCP-HXG	10 km	-6.1	38.0	0.93
ISCCP-HXG	30 km	-5.8	33.9	0.94
ISCCP-HXG	50 km	-6.0	33.4	0.95
ISCCP-HXG	70 km	-5.9	33.3	0.95
ISCCP-HXG	90 km	-5.8	33.1	0.95
ISCCP-HXG	110 km	-6.0	33.4	0.95
ISCCP-FD	280 km	-6.7	51.0	0.87

720



721 **Table 3.** Effect of spatial resolution on accuracy of our estimated daily SSR compared
722 to observations at 90 CMA radiation stations. A comparison with daily SSR
723 of ISCCP-FD is also shown.

	Spatial resolution	MBE (W m^{-2})	RMSE (W m^{-2})	R
ISCCP-HXG	10 km	1.8	32.4	0.93
ISCCP-HXG	30 km	2.1	28.5	0.95
ISCCP-HXG	50 km	2.2	27.4	0.95
ISCCP-HXG	70 km	2.2	27.1	0.95
ISCCP-HXG	90 km	2.1	26.9	0.95
ISCCP-HXG	110 km	2.1	26.9	0.95
ISCCP-FD	280 km	-1.2	36.5	0.91

724



725 **Table 4.** Effect of spatial resolution on accuracy of our estimated monthly SSR
726 compared to observations at 90 CMA radiation stations. A comparison with
727 monthly SSR of ISCCP-FD data is also shown.

	Spatial resolution	MBE (W m^{-2})	RMSE (W m^{-2})	R
ISCCP-HXG	10 km	1.9	16.3	0.97
ISCCP-HXG	30 km	2.2	15.3	0.97
ISCCP-HXG	50 km	2.2	15.0	0.97
ISCCP-HXG	70 km	2.2	14.9	0.97
ISCCP-HXG	90 km	2.2	14.9	0.97
ISCCP-HXG	110 km	2.1	14.8	0.97
ISCCP-FD	280 km	-1.3	20.0	0.95

728